SoftwareX 25 (2024) 101619

Contents lists available at ScienceDirect

SoftwareX

journal homepage: www.elsevier.com/locate/softx

Original software publication

Global-GMDs: The global map of geomagnetic disturbances

Hongyi Hu [a,*], Zhonghua Xu [b]

[a] The Overlake School, Redmond, WA 98040, USA
[b] Center for Space Science and Engineering Research, Virginia Tech, Blacksburg, VA 24061, USA

ARTICLE INFO

Keywords:
Geomagnetic disturbances
Magnetic field measurement
Geomagnetic storm
Geomagnetically induced currents

ABSTRACT

To improve the understanding and monitoring the impacts of geomagnetic disturbances (GMDs) on power grids globally, the presented software, Global-GMDs, uses magnetic field measurements from geomagnetic observatories worldwide and Kriging method to generate global maps of GMDs. It provides better observational information during a solar storm to power grid operations and other crucial infrastructures. It can also help researchers to assess the GMDs prediction model by comparing with Global-GMDs maps and to get better understanding of physics mechanisms.

Code metadata

Current code version	v2
Permanent link to code/repository used for this code version	https://github.com/ElsevierSoftwareX/SOFTX-D-23-00600
Permanent link to Reproducible Capsule	https://github.com/PythonOrC/SpaceWeather-SoftwareX/
Legal Code License	GNU General Public License v3.0
Code versioning system used	git
Software code languages, tools, and services used	Matlab, Matlab Mapping Toolbox Python 3, PIL, glob
Compilation requirements, operating environments	dependencies & Matlab 2022b or above & Python 3
If available Link to developer documentation/manual	https://github.com/PythonOrC/SpaceWeather-SoftwareX
Support email for questions	ethanhu8351@gmail.com zxu77@vt.edu

1. Motivation and significance

Space Weather is the phenomenon of solar storms and other events in space that can have an impact on Earth. The source of space weather is the Sun, which can produce solar flares [1], coronal mass ejections (CMEs) [2], and high-speed solar wind streams [3] that cause significant impacts on modern society [4], affecting technologies such as radio communication, GPS and GNSS systems, and satellite communications, high-latitude aviation, mining operations, power grids, and natural gas pipelines [5]. The geomagnetic disturbances (GMDs) can be generated with a variety of spatial scales during space weather events such as storms or substorms. The Geomagnetically induced currents (GICs) are electric currents induced in power transmission and distribution systems when GMDs induce electric currents in conductive materials, potentially affecting the normal operation of electrical infrastructure. The GICs can cause severe damage to power grids [6,7]. For example, during the 1989 storm [8], the Quebec power grid was out of service within 90 s. The collapsed power grid left six million people and the rest of Quebec without electricity for nine hours in most places, and days in others. This geomagnetic storm caused about $10 million dollars in damage to Quebec and tens of millions of customers out of service. As a result, space weather has significant implications for national security due to the capability to damage critical infrastructures, such as the electric grid. To mitigate these effects, the US has established a Federal Operating Concept for Impending Space Weather Events [9], which focuses on operational and crisis planning.

To find the impacts of GMDs during extreme space weather events, a global GMDs model "Global-GMDs" is developed based on magnetic field data from worldwide distributed magnetometer observatories and the Kriging method [10]. Kriging is a geostatistical interpolation method used in spatial data analysis to estimate values at unobserved locations based on known data points [11]. It considers the spatial correlation and variability of data to provide the best linear unbiased predictions, making it valuable in applications such as

* Corresponding author.
E-mail addresses: ethanhu8351@gmail.com (Hongyi Hu), zxu77@vt.edu (Zhonghua Xu).

https://doi.org/10.1016/j.softx.2023.101619
Received 8 September 2023; Received in revised form 7 December 2023; Accepted 11 December 2023
Available online 22 December 2023

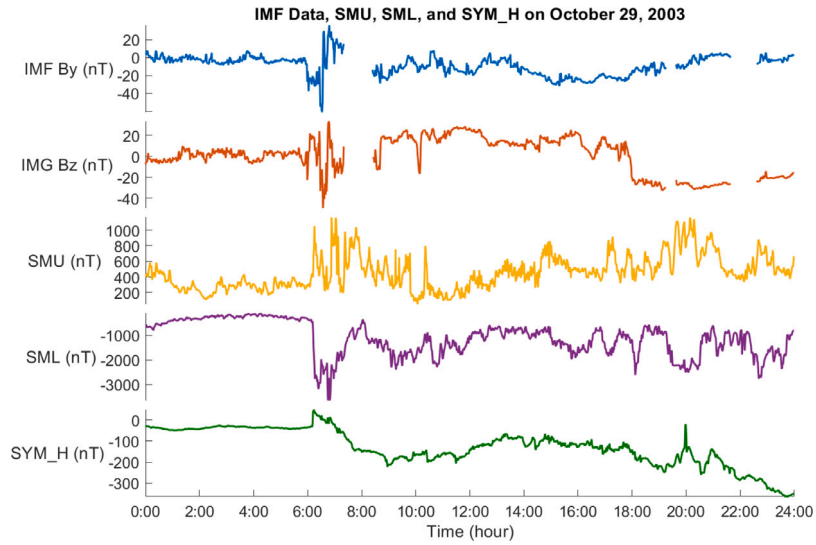

Fig. 1. IMF, SMU, SML, and SYM_H Data of Oct. 29, 2003. The gaps in the IMF By & Bz plot represent missing data.

environmental modeling, geology, and spatial statistics. Magnetometers have been proven essential in this area for both research and monitoring. It is important to use magnetometer observation to investigate the physics mechanism behind GMDs and GICs to verify the model predictions with observations [12]. Most of the study has been done with regional focuses [13–15], while this new GMDs model focuses on adapting all the available magnetometer data into one model to provide the best global coverage. Examining the GMDs global maps provides better observational information during a solar storm to power grid operations and other crucial infrastructures [16]. For historical events, the global maps provide a better understanding of how GMDs affect power grids. During a live GMD event, the global maps could show the development and the trend of the impact locations. Also, by comparing the predicted value of geomagnetic disturbances to global maps, researchers can assess the prediction's accuracy and how the model can be improved to achieve better and more accurate results.

2. Software description

The Global-GMDs model is based on geomagnetic data from over 200 geomagnetic observatories collected during the Halloween Storm and Kriging method, which makes it possible to draw a global picture of the storm's impacts on geomagnetic disturbances. The 2003 Halloween Storm was picked because it was the strongest solar storm in the last three decades. The "Halloween Storm" refers to a severe geomagnetic storm that occurred on October 29, 2003. This storm was not directly related to the Halloween holiday but earned its name because of its occurrence during the same time period. It was a result of a powerful solar flare and a coronal mass ejection (CME) from the Sun. Since the Halloween storm lasted three days and had several waves of storms, the first storm (Storm-1) is picked as the example period to show the strength of the model. Storm-1 is defined as the period between 06:11 - 08:03 UTC, Oct. 29, 2003, based on the level of Interplanetary Magnetic Field (IMF) based on observations from ACE Satellite, SMU/SML, and Sym-H indices shown in Fig. 1. Solar wind data are from ACE satellites in the NASA database.[1] The Interplanetary Magnetic Field (IMF) data are split into three components in the Geocentric Solar Magnetospheric (GSM) coordinate. The SMU/SML data are from SuperMAG.[2] [17] The SYM-H data are from the World Data Center for Geomagnetism, Kyoto.[3]

The SMU/L indices are magnetic indices derived from the magnetometer data provided by the SuperMAG collaborators. SMU stands for SuperMAG Upper envelope of N-component for stations between 40° and 80° magnetic north, while SML stands for SuperMAG Lower envelope of N-component for stations between 40° and 80° magnetic north. These indices are similar to the official AU/AL indices at the World Data Center for Geomagnetism, Kyoto. The Sym-H, standing for Symmetric disturbance field in H, the index is essentially the same as Sugiura's hourly Dst index [18], but using 1-minute values from different sets of stations and a slightly different coordinate system [19].

Magnetic Variation Data with a time resolution of one minute and a time interval from 00:00 UT to 23:59 UT, October 29, 2003, was downloaded from SuperMAG (supermag.jhuapl.edu). The instruction for downloading the data is included in the C8 Documentations.[4] The magnetic field data are in three components: dBn is the N-direction component of local magnetic north, dBe is the E-direction component of local magnetic east, and dBz is the Z-direction of vertically down. The baseline of daily variations and yearly trends has been subtracted by SuperMAG [20]. Stations containing more than 20 min of missing data during the time of interest (Storm-1: 06:11 - 08:03 UTC, Oct. 29, 2003) are then removed due to inaccurate interpolation. This leaves 193 quality stations for Storm-1.

2.1. Software architecture

The magnetic variation data are then used to generate the global maps of magnetic variations during the defined Storm-1, which are created with MATLAB. There are two parts to the program as shown in Fig. 2, the first is data preparation while the second is data visualization. All software, figures, and data for this study are available on GitHub.[5]

The purpose of data preparation is to create organized data structures that can be used to visualize storms easily. The magnetic variation data from SuperMAG and the IMF data from NASA are loaded separately, then stored in two data tables "LOC" and "OBS" (shown in Fig. 2). The data table "LOC" is used to display the "LOCation marks" on global maps, including the geographical coordinates, magnetic local time (MLT), and a numerical station ID. Data table "OBS", used to generate the global colormap, includes station information (IAGA code,

[1] https://sohoftp.nascom.nasa.gov/sdb/goes/ace/daily/
[2] https://supermag.jhuapl.edu/indices/
[3] https://wdc.kugi.kyoto-u.ac.jp/aeasy/index.html
[4] https://github.com/PythonOrC/SpaceWeather-SoftwareX
[5] https://github.com/PythonOrC/SpaceWeather-SoftwareX

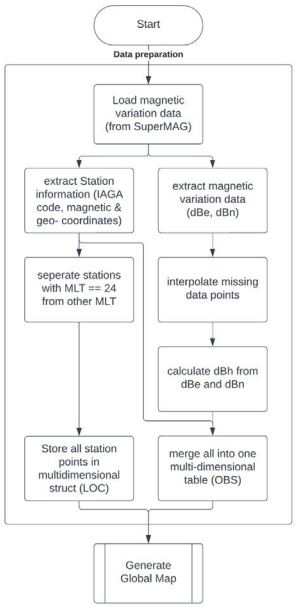

(a) Data Preparation Part of Code

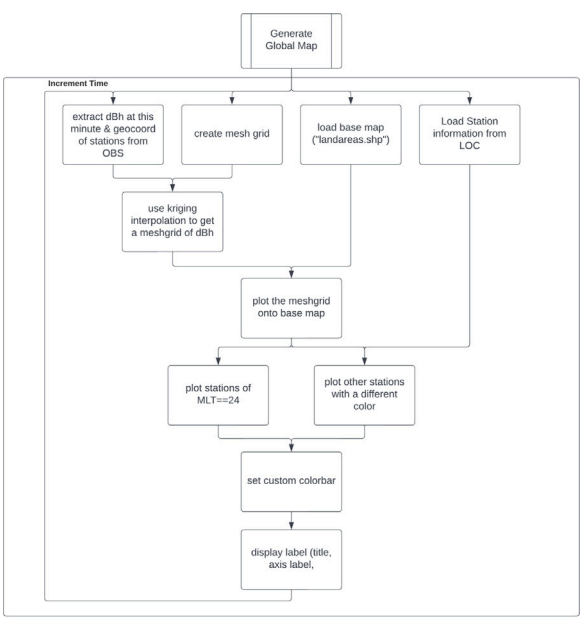

(b) Data Visualization Part of Code

Fig. 2. Model flowchart.

magnetic and geographical coordinates), and magnetic variation data (dBn, dBe, and dBh).

Once the station location information is extracted to "LOC", the stations are stored in a $\{2 \times n\ cell\}$ cell where n represents the length of the storm in minutes for displaying station marks on the map. The first row of the table represents stations that are near MLT midnight, while the second row represents the stations that are at other MLTs. Then, the stations near MLT midnight can be graphed differently than the other stations on the map later. An example of this structure is as follows (see Table 1):

Each cell has a max size of $\{1 \times 18\ cell\}$, where the number 18 is determined by the 10° magnetic latitude chunks between [−90 90]. The stations are separated into these chunks to alternate colors of the stations in every chunk where chunk size equals 10°.

Table 1
Structure in data table "LOC".

Time (min)	1	2	...	n
MLT == 24	1 × 18 cell	1 × 18 cell	1 × 18 cell	1 × 18 cell
MLT != 24	1 × 18 cell	1 × 18 cell	1 × 18 cell	1 × 18 cell

Table 2
Data structure for storing stations by 10° magnetic latitude chunks.

MagLat	−90 to −80	−79 to −70	−69 to −60	...	81 to 90
Stations	1 × 2 double	1 × 9 double	1 × 8 double	...	1 × 6 double

Table 3
Data structure for storing station information in each magnetic latitude chunk.

Geometry	Lat	Lon	StationID
'Point'	−66.28	110.53	46
'Point'	−66.67	140.01	56

The number of magnetic latitude chunks (m) can be found with

$$m = \frac{180°}{MAGLAT\_CHUNK\_SIZE}$$

A given cell might look like the following (see Table 2):

Each of the x entries inside the cells contains four fields (Geometry, Lat, Lon, and StationID). Geometry only exists to satisfy the parameter requirements of the geoshow() function used in data visualization and always has 'Point' as the value. Lat and Lon are used to locate the station while StationID is used to identify which station this point represents. For example, the $\{1 \times 2\ double\}$ cell between [−90 −80] looks like the following (see Table 3).

When the magnetic variation data are extracted, the missing points are linearly interpolated before calculating the dBh value. The signage of the value is then based on the signage of the dBn value (positive dBn means a positive dBh).

$$\mathrm{dBh} = \frac{|\mathrm{dBn}|}{\mathrm{dBn}} \times \sqrt{\mathrm{dBn}^2 + \mathrm{dBe}^2}$$

To better visualize the impact on GIC, an option in the program also allows the time derivative of dbh (derivative_dBh) to be plotted with the following equation where diff() refers to the difference of the value between two consecutive time frames [21].

$$\mathrm{derivative\_dBh} = \sqrt{\mathrm{diff}(\mathrm{dBn})^2 + \mathrm{diff}(\mathrm{dBe})^2}$$

Then, the IAGA code, latitude, longitude, dBn, dBe, and dBh are all stored in a single multidimensional table named "OBS". This is the table used to create the global colormap. Thus, data preparation has finished and these processed data are then visualized.

To visualize the data as global colormaps, a mesh grid is first created with a precision of 0.5° in geographical coordinates. The dBh value for all stations at this particular minute is obtained from OBS and then interpolated using the Kriging method, incorporating the geographic coordinates from OBS into the mesh grid. The opensource matlab programs `kriging.m`, `variogram.m`, `variogramfit.m`, and `fminsearchbnd.m` used in the code is from Wolfgang Schwanghart and John D'Errico [22–25]. This mesh grid is then overlaid onto the base map `landareas.shp` loaded from the Mapping Toolbox in MATLAB. Next, using the station information for this minute extracted from "LOC," the magnetic locations of the stations are represented as circular marks. These marks alternate between black and white every 10 degrees. The stations near MLT midnight are plotted as a purple diamond. A custom color bar is configured to accentuate variations in lower numerical values.

The figure includes labels, color bar markings, axis labels, and titles that display the date and time. Finally, the figure is saved as a PNG file in a designated folder.

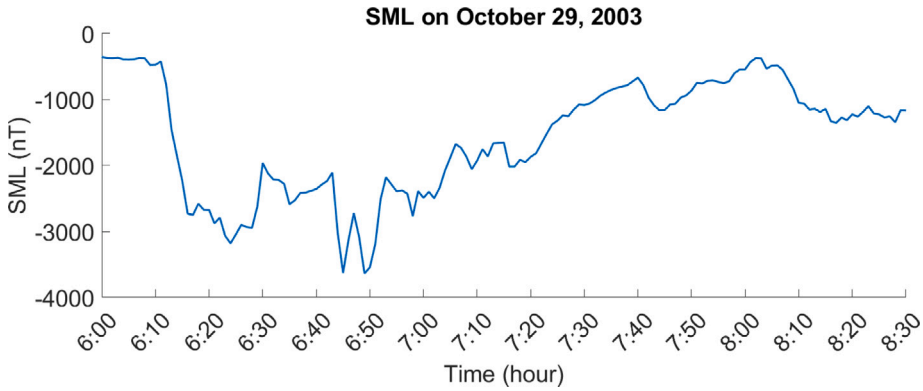

Fig. 3. SML Zoomed In At The Storm-1.

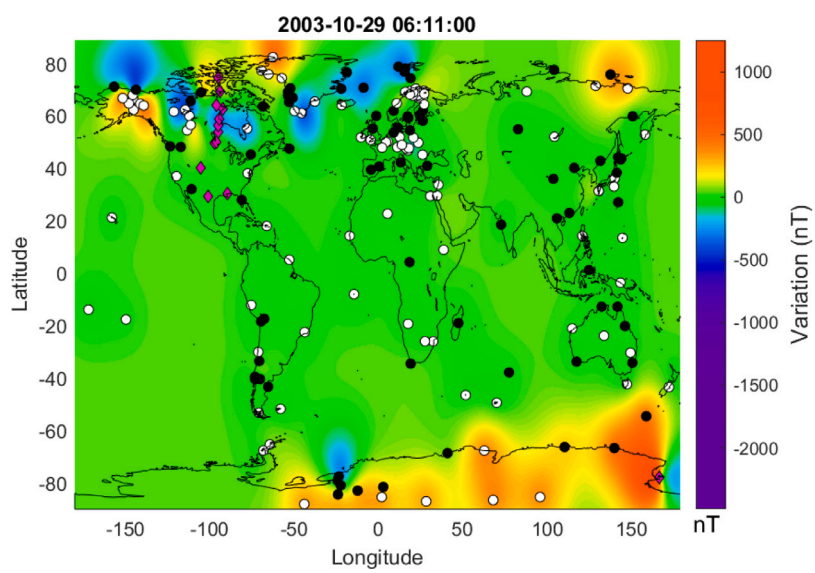

Fig. 4. Global Map of GMDs At UTC 6:11 in geographic coordinates.

2.2. Software functionalities

The major functionality of this program is to offer a visualization tool that enables researchers studying specific magnetic storms to observe the storm on a global scale and zoom in to examine localized impacts. It utilizes global GMD maps to identify affected regions and trace the propagation of these effects. Additionally, the program includes markers on the map to indicate the geographic distribution of observatories.

3. Illustrative examples

By checking the zoom-in SML index shown in Fig. 3 while looking at the global colormap of GMDs, it can be seen that the first storm on Oct. 29th, 2003 started at 06:11 UT with a negative change. The global map of GMDs at 06:11UT shown in Fig. 4 shows traces of GMDs near auroral zone around Alaska, Canada, Greenland, Iceland, and Svalbard. The max intensity is around $\pm 400nT$.

In just 5 min at 06:16 UT, the storm increased in both intensity and size, as shown in Fig. 5. In the northern hemisphere, the storm propagated to northern parts of Europe (near Finland and Norway), reaching a max intensity of around $+1000nT$ and $-1500nT$. In the southern hemisphere, the storm was observed with an increasing intensity near station B15 (m82-003, magnetic longitude 36.68°, magnetic latitude −68.39°). This indicates an enhancement of the storm.

Then, as shown in Fig. 6, by 06:49 UT, the storm had impacted all of the high latitudes and expanded to lower latitudes in both hemispheres (near Germany, Denmark, Poland, and the northern UK in the northern hemisphere and near the South Atlantic Ocean and B04 (m68-041, magnetic longitude 73.59°, magnetic latitude −65.98°) in the Southern Hemisphere). It even has some impacts on the equatorial regions such as Africa with an intensity of around −250 nT, which is uncommonly disturbed for equatorial regions. The strongest dBh is less than −2800 nT and more than 1500 nT.

Finally, at 08:03 UT, the regions have mostly recovered from the storm impact with some minor localized variations in the high and mid-latitude regions, as shown in Fig. 7.

4. Model validation

By these examples during Storm-1, the global maps of GMDs present a big picture that shows where the impacts first occurred on the Earth, how the regions of impact expanded, and how intense the impacts were. In order to quantitatively valid the model's effectiveness, the kriging results are compared to observations as follows: 1. remove one station from the list; 2. interpolate the global GMDs by using the data from the

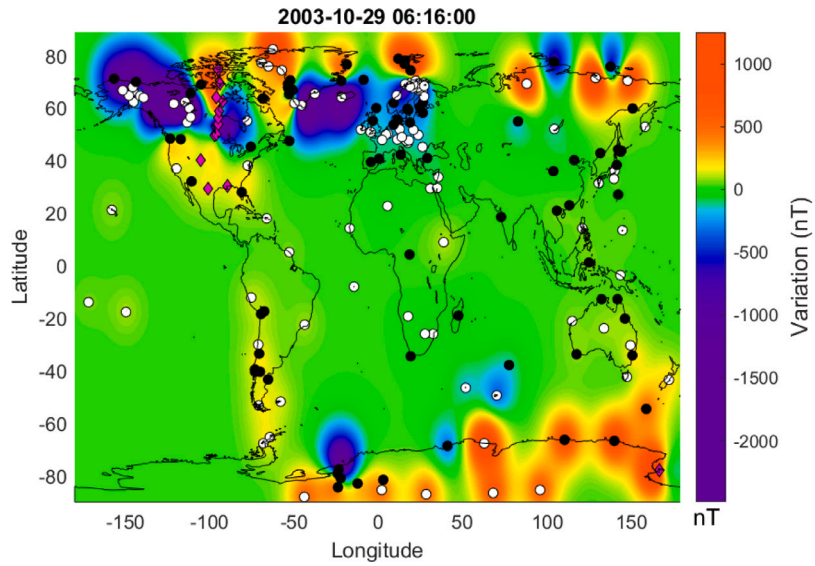

Fig. 5. Global Map of GMDs At UTC 6:16 in geographic coordinates. (For interpretation of the references to color in this figure legend, the reader is referred to the web version of this article.)

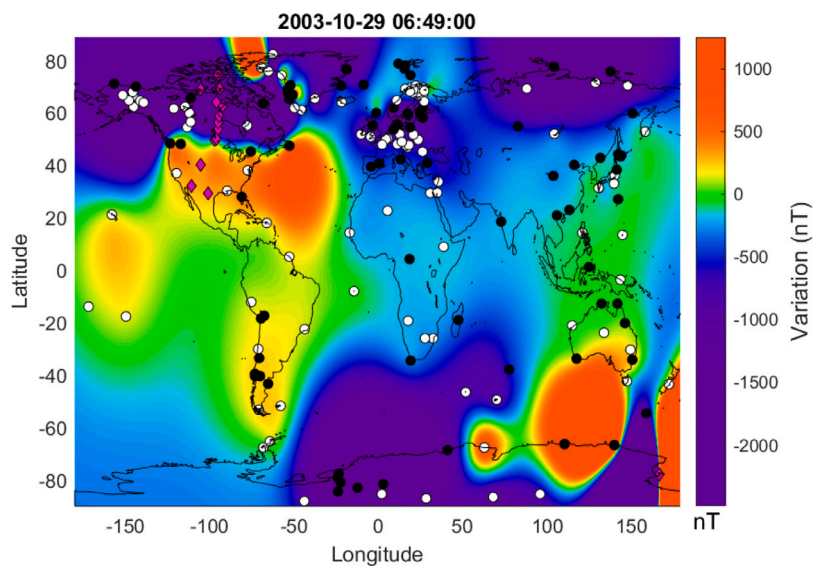

Fig. 6. Global Map of GMDs At UTC 6:49 in geographic coordinates. (For interpretation of the references to color in this figure legend, the reader is referred to the web version of this article.)

rest of the stations; 3. save the interpolated data where the removed station is; 4. repeat 2-3 for every minute of the storm; 5. repeat 1-4 for every station.

Next, the interpolated data and the original observations from the station are analyzed from two different perspectives. The first angle assesses how geographical location affects the accuracy of the interpolation, while the second angle examines how storm intensity influences accuracy. These validation data are available on GitHub.

4.1. Impact of geographical location

To analyze the impacts of the storm, the Mean Absolute Error (MAE) of each station is calculated, and the relative percentage of it (Relative MAE) to the max value is then calculated.

$$MAE = \frac{1}{n}\sum_{i=0}^{m} |x_i - \hat{x}_i|$$

$$Relative\ MAE = \frac{MAE}{x_{\max}}$$

where the x_i is the real dBh value of the station at time i, $\hat{x}_i$ is the interpolated value of the station at time i, and $x_{\max}$ is the maximum actual dBh value of the station during the period.

These percentage errors are then divided into three categories of accuracy and plotted on a world map. The first category is plotted with a green dot, representing a percentage error between 0% and 15%. The second category is plotted with a yellow dot, representing a percentage error between 15% and 45%. Any station with a larger error than 45%

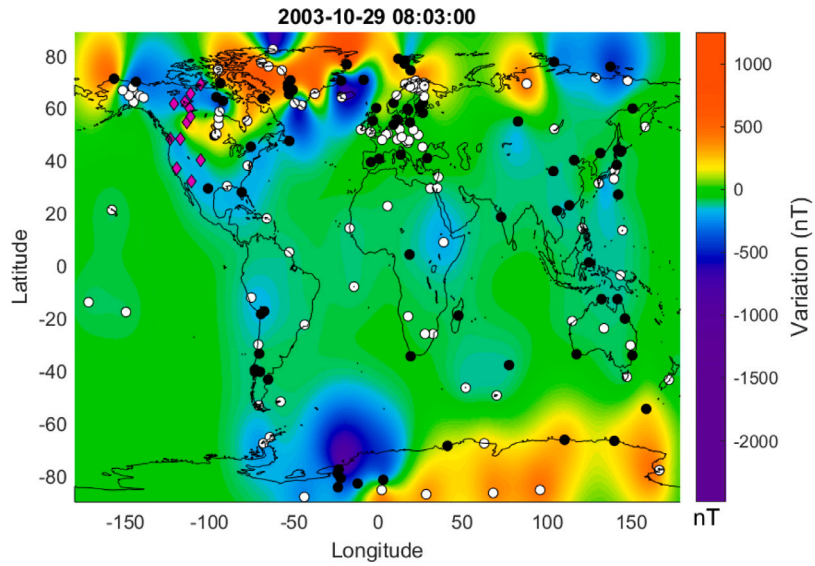

Fig. 7. Global Map of GMDs At UTC 8:03 in geographic coordinates.

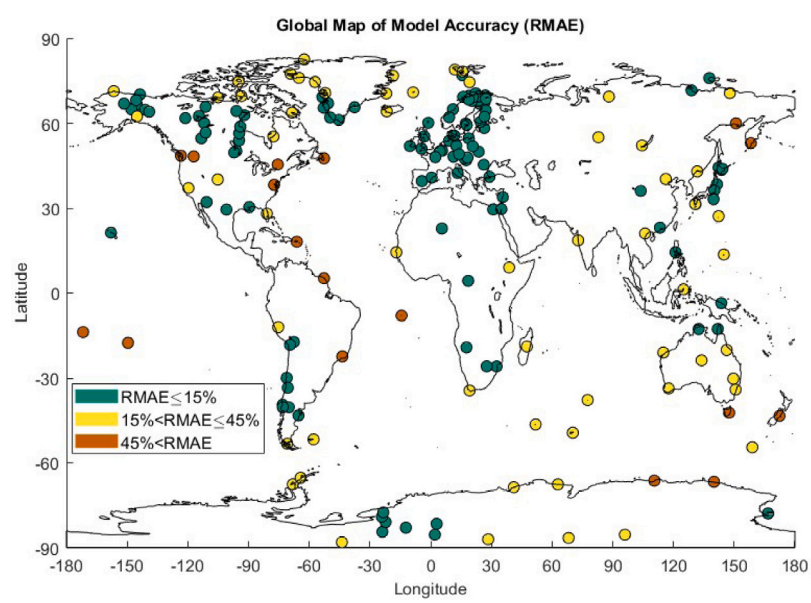

Fig. 8. Global map of model accuracy validation. Stations of green dots have (Relative MAE) errors ≤ 15%; yellow dots, errors > 15% and ≤ 45%; red dots, errors > 45%. (For interpretation of the references to color in this figure legend, the reader is referred to the web version of this article.)

is then plotted with a red dot. Out of the 193 stations available to this storm, 116 stations (60.1%) have an error ≤ 15%; 60 stations (31.1%) have an error > 15% and ≤ 45%; 17 stations (8.8%) have an error > 45%.

The varying levels of accuracy in interpolated Geomagnetic Disturbance (GMD) data across different latitude regions are depicted in Fig. 8. Interpolated GMDs achieve an acceptable level of accuracy, which is indicated by green (Relative MAE between 0% and 15%) and yellow (Relative MAE between 15% and 45%) colors. Notably, in lower latitude regions of Africa and Asia, fewer monitoring stations suffice to attain this level of accuracy compared to higher latitude areas. However, in the lower latitude areas of the Americas and oceans, the interpolated GMDs exhibit lower accuracy. In mid-latitude regions, the accuracy of the interpolated GMDs at US continental stations is lower, as shown by the red dots. In high-latitude regions, typically considered the most affected areas during magnetic storms, the interpolated GMDs demonstrate good accuracy, as indicated by the green and yellow dots.

Given that the level of GMD disturbances is strongest in high-latitude regions, weaker in mid-latitude areas, and weakest in low-latitude regions (as shown in Fig. 6), a higher density of ground observatories significantly enhances the accuracy of GMD interpolations in high-latitude regions, where these disturbances have the most significant impact. This is particularly evident in regions such as Europe and Canada. In contrast, areas with fewer observatories, like those in oceanic regions and continental U.S. stations, experience a decrease in the accuracy of GMD interpolations as the distance from these stations increases. One possible explanation for this trend is that Weygand and others [26] reported full-width half maximum radii of GMDs between 250–450 km. When considering both latitude and observatory density

as contributing factors, a higher density of spatial magnetometers is necessary to achieve a comparable level of accuracy in high-latitude regions. While fewer magnetometer observatories are needed in mid- and lower-latitude regions compared to high-latitude regions, the current spatial coverage remains insufficient in mid- and low-latitude areas.

4.2. Impact of storm intensity

To analyze the impact of storm intensity on interpolation accuracy, Absolute Errors (AEs) for each station are examined as a time series for each minute during the Storm-1 period. The overall trend reveals greater errors during periods of heightened magnetic disturbances. The most significant AEs occur during the peak of the largest magnetic disturbance, approximately at 07:40 UTC. Notably, the AEs at LOV (Lovo, magnetic longitude 96.06°, magnetic latitude 55.74°) station consistently remain low throughout the Storm-1 period, with only a few exceptions. This observation is particularly significant because LOV is centrally located within a region densely populated with magnetic observatories in Europe. This pattern implies that the model's accuracy is largely dependent on the extent of spatial coverage provided by magnetic observations within the region.

Overall, the model validation reveals that the accuracy of interpolated GMDs is influenced by geographical locations, observatory density, and GMD intensity during the storms. This relationship is more intricate than simply the distance from the observatory and warrants further investigation. Our next phase of research will delve into how the density of magnetometer observatories and the specific geographic coordinates impact the interpolation results.

5. Impact

The Global-GMDs model offers a global perspective on the progression of the storm over time, clearly identifying its inception, propagation, peak, and recovery phases. This model provides high spatial resolution (0.5 degrees), high time resolution (1-minute), and relatively accurate observational data for the Halloween Storm of 2003 on a global scale. The global GMD map reveals that the 2003 Halloween Storm began in the Aurora zone, encompassing regions like Alaska, Canada, Greenland, Iceland, and Svalbard. It intensified as it propagated toward mid-latitude regions such as Germany, France, and the USA, with increased intensity in high latitudes. Eventually, the storm reached its maximum intensity, causing significant magnetic fluctuations in high latitudes and extending to lower latitudes, including normally quiet equatorial zones. Subsequently, most regions recovered from the storm's impact, leaving minor localized variations in high and mid-latitude regions. Furthermore, the global map allows us to discern regional features and assess the extent of localized impact, connecting them to the effects of GMDs on power grids. GICs are secondary currents in power system grids induced by the strong GMDs. The GICs do not cause damage to the transmission lines themselves, they can damage transformers through thermal damage that causes them to age rapidly if not fail immediately.[27]. For instance, regions like Sweden [28] and South Africa [29], which exhibited strong impacts on the global maps, experienced power grid failures and hours-long power outages. To be noted, strong GMDs alone are not enough to cause high GICs and power failures, like Canada at 6:49 UT shown in Fig. 6. It also depends on the ground conductivity, power grid conditions, operations, and other factors.

Overall, the model proves sufficiently accurate GMDs during the storm. However, accuracy varies significantly across regions, depending on three factors: the localization of features, the intensity of variations, and the density of observation stations. Regions with high latitudes characterized by intense and localized variations require more observatories for accurate GMDs, whereas quieter regions like the equatorial zones require fewer stations.

The next step is a quantitative investigation to determine station spatial coverage requirements, considering errors resulting from geographical locations, observatory density, and GMD intensity during magnetic storms. Additionally, potential research includes utilizing the model to display the spatial distribution of magnetic pulsations filtered at specific frequencies, like Ultra Low-Frequency wave Pc5, which can potentially lead to hazardous GICs affecting power grids [30]. Over the last decade, the US government has developed a series of government reports and national action plans [16]. Combining these maps with other GIS databases could facilitate space weather impact assessments not only for power grid operations but also for critical infrastructures, including hospitals, financial centers, emergency response systems, and national security-related agencies.

6. Conclusions

In order to enhance the understanding and surveillance of the effects of geomagnetic disturbances (GMDs) on power grids around the world, the software known as Global-GMDs is developed by utilizing magnetic field data collected from geomagnetic observatories across the globe and employing the Kriging method to create comprehensive global maps of GMDs. This valuable tool furnishes improved observational data during solar storms, benefiting power grid operators and other vital infrastructure stakeholders. Furthermore, it aids researchers in evaluating GMDs prediction models by enabling them to compare their models with the maps generated by Global-GMDs, facilitating a deeper understanding of the underlying physics mechanisms.

Declaration of competing interest

The authors declare that they have no known competing financial interests or personal relationships that could have appeared to influence the work reported in this paper.

Data availability

Data will be made available on request.

Acknowledgments

For the ground magnetometer data, we gratefully acknowledge the SuperMAG[6] and its collaborators: INTERMAGNET, Alan Thomson; CARISMA, PI Ian Mann; CANMOS, Geomagnetism Unit of the Geological Survey of Canada; The S-RAMP Database, PI K. Yumoto and Dr. K. Shiokawa; The SPIDR database; AARI, PI Oleg Troshichev; The MACCS program, PI M. Engebretson; GIMA; MEASURE, UCLA IGPP and Florida Institute of Technology; SAMBA, PI Eftyhia Zesta; 210 Chain, PI K. Yumoto; SAMNET, PI Farideh Honary; IMAGE, PI Liisa Juusola; Finnish Meteorological Institute, PI Liisa Juusola; Sodankylä Geophysical Observatory, PI Tero Raita; UiT the Arctic University of Norway, TromsøGeophysical Observatory, PI Magnar G. Johnsen; GFZ German Research Centre For Geosciences, PI Jürgen Matzka; Institute of Geophysics, Polish Academy of Sciences, PI Anne Neska and Jan Reda; Polar Geophysical Institute, PI Alexander Yahnin and Yarolav Sakharov; Geological Survey of Sweden, PI Gerhard Schwarz; Swedish Institute of Space Physics, PI Masatoshi Yamauchi; AUTUMN, PI Martin Connors; DTU Space, Thom Edwards and PI Anna Willer; South Pole and McMurdo Magnetometer, PI's Louis J. Lanzarotti and Alan T. Weatherwax; ICESTAR; RAPIDMAG; British Artarctic Survey; McMac, PI Dr. Peter Chi; BGS, PI Dr. Susan Macmillan; Pushkov Institute of Terrestrial Magnetism, Ionosphere and Radio Wave Propagation (IZMIRAN); MFGI, PI B. Heilig; Institute of Geophysics, Polish Academy of Sciences, PI Anne Neska and Jan Reda; University of L'Aquila, PI

[6] https://supermag.jhuapl.edu/info/?page=acknowledgement

M. Vellante; BCMT, V. Lesur and A. Chambodut; Data obtained in cooperation with Geoscience Australia, PI Andrew Lewis; AALPIP, co-PIs Bob Clauer, Michael Hartinger, and Zhonghua Xu; MagStar, PI Jennifer Gannon; SuperMAG, PI Jesper W. Gjerloev; Data obtained in cooperation with the Australian Bureau of Meteorology, PI Richard Marshall. For the solar wind and IMF data, we gratefully acknowledge the NASA Solar and Heliospheric Observatory (SOHO) Project website.[7]

References

[1] Kusano K, Bamba Y, Yamamoto TT, Iida Y, Toriumi S, Asai A. Magnetic field structures triggering solar flares and coronal mass ejections. Astrophys J 2012;760(1):31. http://dx.doi.org/10.1088/0004-637x/760/1/31.

[2] Hathaway DH, Wilson RM. Geomagnetic activity indicates large amplitude for sunspot cycle 24. Geophys Res Lett 2006;33.

[3] Tsurutani BT, McPherron RL, Gonzalez WD, Lu G, Gopalswamy N, Guarnieri FL. Magnetic storms caused by corotating solar wind streams. In: Recurrent magnetic storms: Corotating solar wind streams. American Geophysical Union (AGU); 2006, p. 1–17. http://dx.doi.org/10.1029/167GM03, arXiv:https://agupubs.onlinelibrary.wiley.com/doi/pdf/10.1029/167GM03, URL https://agupubs.onlinelibrary.wiley.com/doi/abs/10.1029/167GM03.

[4] Eastwood JP, Biffis E, Hapgood MA, Green L, Bisi MM, Bentley RD, et al. The economic impact of space weather: Where do we stand? Risk Anal 2017;37(2):206–18. http://dx.doi.org/10.1111/risa.12765.

[5] Berger TE, Holzinger MJ, Sutton EK, Thayer JP. Flying through uncertainty. Space Weather 2020;18(1). http://dx.doi.org/10.1029/2019SW002373, e2019SW002373.

[6] Pulkkinen A, Bernabeu E, Thomson A, Viljanen A, Pirjola R, Boteler D, et al. Geomagnetically induced currents: Science, engineering, and applications readiness. Space Weather 2017;15(7):828–56. http://dx.doi.org/10.1002/2016SW001501, arXiv:https://agupubs.onlinelibrary.wiley.com/doi/pdf/10.1002/2016SW001501.

[7] Gannon J. In: Gannon JL, Swidinsky A, Xu Z, editors. Geomagnetically induced currents from the sun to the power grid. Geophysical monograph series, Nashville, TN: John Wiley & Sons; 2019.

[8] Boteler DH. A 21st century view of the March 1989 magnetic storm. Space Weather 2019;17(10):1427–41. http://dx.doi.org/10.1029/2019SW002278.

[9] FEMA Homeland Security. Federal operating concept for impending space weather events. 2019, URL https://www.fema.gov/sites/default/files/2020-07/fema_incident-annex_space-weather.pdf.

[10] Xu Z, Gannon JL, Rigler EJ. Report of geomagnetic pulsation indices for space weather applications: U.S. Geological survey open-file report 2013-1166. 2013, p. 22, URL http://pubs.usgs.gov/of/2013/1166/.

[11] Matheron G. Principles of geostatistics. Econ Geol 1963;58(8):1246–66. http://dx.doi.org/10.2113/gsecongeo.58.8.1246, arXiv:https://pubs.geoscienceworld.org/segweb/economicgeology/article-pdf/58/8/1246/3481854/1246.pdf.

[12] Kotzé PB, Cilliers PJ, Sutcliffe PR. The role of SANSA's geomagnetic observation network in space weather monitoring: A review. Space Weather 2015;13(10):656–64. http://dx.doi.org/10.1002/2015SW001279.

[13] Barbosa CS, Alves LR, Caraballo R, Hartmann GA, Papa ARR, Pirjola RJ. Analysis of geomagnetically induced currents at a low-latitude region over the solar cycles 23 and 24: Comparison between measurements and calculations. J Space Weather Space Clim 2015;5.

[14] Batista IS, Abdu MA, de Souza JR, Bertoni FCP, Matsuoka MT, de Oliveira Camargo P, et al. Unusual early morning development of the equatorial anomaly in the Brazilian sector during the Halloween magnetic storm. J Geophys Res 2006;111:10.

[15] Schultz C. Solar storms can destabilize power grids at midlatitudes. EOS Trans Am Geophys Union 2012;93(41):412. http://dx.doi.org/10.1029/2012EO410020.

[16] National space weather strategy and action plan. 2019, URL https://trumpwhitehouse.archives.gov/wp-content/uploads/2019/03/National-Space-Weather-Strategy-and-Action-Plan-2019.pdf.

[17] Newell PT, Gjerloev JW. Evaluation of SuperMAG auroral electrojet indices as indicators of substorms and auroral power. J Geophys Res Space Phys 2011;116(A12). http://dx.doi.org/10.1029/2011JA016779, arXiv:https://agupubs.onlinelibrary.wiley.com/doi/pdf/10.1029/2011JA016779, URL https://agupubs.onlinelibrary.wiley.com/doi/abs/10.1029/2011JA016779.

[18] Poros DJ, Sugiura M. Hourly values of equatorial Dst, 1957 - 1970. 1971, GSFC Doc NASA-TM-X-65645, NASA Goddard Space Flight Center, URL https://ntrs.nasa.gov/citations/19710022962.

[19] Iyemori T, Takeda M, Nose M, Odagi Y, Toh H. Mid-latitude geomagnetic indices ASY and SYM for 2009 (Provisional). In: Internal report of data analysis center for geomagnetism and space magnetism. Japan: Kyoto University; 2010, URL https://wdc.kugi.kyoto-u.ac.jp/aeasy/asy.pdf.

[20] Gjerloev JW. The SuperMAG data processing technique. J Geophys Res Space Phys 2012;117(A9). http://dx.doi.org/10.1029/2012JA017683.

[21] Viljanen A, Nevanlinna H, Pajunpää K, Pulkkinen A. Time derivative of the horizontal geomagnetic field as an activity indicator. Ann Geophys 2001;19(9):1107–18. http://dx.doi.org/10.5194/angeo-19-1107-2001, URL https://angeo.copernicus.org/articles/19/1107/2001/.

[22] Schwanghart W. Experimental (semi-) variogram. MATLAB Central File Exchange, URL https://www.mathworks.com/matlabcentral/fileexchange/20355-experimental-semi-variogram.

[23] Schwanghart W. variogramfit. MATLAB Central File Exchange, URL https://www.mathworks.com/matlabcentral/fileexchange/25948-variogramfit.

[24] Schwanghart W. Ordinary kriging. MATLAB Central File Exchange, URL https://www.mathworks.com/matlabcentral/fileexchange/29025-ordinary-kriging.

[25] D'Errico J. fminsearchbnd, fminsearchcon. MATLAB Central File Exchange, URL https://www.mathworks.com/matlabcentral/fileexchange/8277-fminsearchbnd-fminsearchcon.

[26] Weygand JM, Engebretson MJ, Pilipenko VA, Steinmetz ES, Moldwin MB, Connors MG, et al. SECS analysis of nighttime magnetic perturbation events observed in arctic Canada. J Geophys Res Space Phys 2021;126(11). http://dx.doi.org/10.1029/2021JA029839, arXiv:https://agupubs.onlinelibrary.wiley.com/doi/pdf/10.1029/2021JA029839, URL https://agupubs.onlinelibrary.wiley.com/doi/abs/10.1029/2021JA029839, e2021JA029839 2021JA029839.

[27] Oyedokun DT, Cilliers PJ. Chapter 16 - Geomagnetically induced currents: A threat to modern power systems. In: Zobaa AF, Abdel Aleem SH, Abdelaziz AY, editors. Classical and recent aspects of power system optimization. Academic Press; 2018, p. 421–62. http://dx.doi.org/10.1016/B978-0-12-812441-3.00016-1, URL https://www.sciencedirect.com/science/article/pii/B9780128124413000161.

[28] Pulkkinen A, Lindahl S, Viljanen A, Pirjola R. Geomagnetic storm of 29–31 October 2003: Geomagnetically induced currents and their relation to problems in the Swedish high-voltage power transmission system. Space Weather 2005;3(8). http://dx.doi.org/10.1029/2004SW000123, arXiv:https://agupubs.onlinelibrary.wiley.com/doi/pdf/10.1029/2004SW000123, URL https://agupubs.onlinelibrary.wiley.com/doi/abs/10.1029/2004SW000123.

[29] Agency SANS. Protecting South Africa's power lines from the Sun. 2018, https://www.sansa.org.za/2018/11/14/protecting-south-africas-power-lines-from-the-sun/. [Accessed 29 October 2023].

[30] Hartinger MD, Shi X, Rodger CJ, Fujii I, Rigler EJ, Kappler K, et al. Determining ULF wave contributions to geomagnetically induced currents: The important role of sampling rate. Space Weather 2023;21(5). http://dx.doi.org/10.1029/2022SW003340, arXiv:https://agupubs.onlinelibrary.wiley.com/doi/pdf/10.1029/2022SW003340, URL https://agupubs.onlinelibrary.wiley.com/doi/abs/10.1029/2022SW003340, e2022SW003340 2022SW003340.

[7] https://sohoftp.nascom.nasa.gov/sdb/goes/ace/daily/